Numerical modelling of plate anchors under sustained load: The enhancement of capacity from consolidation

K.A. Kwa , D.J. White

University of Southampton Southampton, SO17 1BJ, UK

A B S T R A C T

Embedded plate anchors can be used to moor floating offshore facilities. In taut mooring systems, a sustained tension carried by the anchors affects their long-term capacity due to consolidation effects in the soil surrounding the anchor. The resulting gain in capacity provides a potential basis for more efficient anchoring system design. To quantify this effect, and to understand the underlying mechanism, a systematic numerical study has been performed, to capture the effect of sustained loading and consolidation on soil failure mechanisms around an embedded plate anchor. The modified Cam clay model is used, to capture the effect of consolidation on soil strength, and also to faithfully model the process by which a water-filled gap forms under the plate, due to a loss of contact between the plate and the soil, with seepage into the gap zone. A critical observation is the load transfer process when such a gap forms beneath the plate after the applied tension causes the effective stress to fall to zero. The formation of this gap is shown to depend, in a systematic way, on the sustained tension, or preload, the soil strength ratio, the relative sharing of the anchor load between compression above the plate and tension below, as well as the embedded depth of the anchor. Simple relationships that capture these mechanisms are provided, linking the net change in soil strength above and below the anchor to the change in undrained capacity. As an example, it is shown that in soft normally-consolidated clays, a sustained preload of 60 % of the initial capacity, can create a 25 % gain in capacity, at which point the factor of safety is raised from $1/0.6 = 1.67$ to 2. This gain is only available for anchors embedded by more than twice their diameter. At shallower embedment, the loss of strength in the unloaded soil beneath the anchor outweighs the gain in strength in the smaller zone of soil above the anchor, and the consolidation process causes a net weakening.

1. Introduction

1.1. Background

Embedded plate anchor mooring systems are an efficient and versatile foundation solution for floating offshore facilities. They provide high capacity relative to their self-weight, and they can be installed by drag-embedment, free-fall, screwing or via a suction anchor (Randolph et al., 2011; Aubeny 2017; O'Loughlin et al. 2017; Cerfontaine et al. 2023). The mooring tension is then applied via a chain or cable system directly to the plate or an attached shank (or in the case of a screw anchor, to the cylindrical shaft).

In soft soils, the anchor capacity can vary with time due to the sustained and variable components of the anchor loads, which are affected by seastate, season, and the operational or ballasting condition of the floating system. In mooring systems with taut mooring lines, there is always a sustained level of tension carried at the anchor plate. The long-term capacity of an embedded plate anchor may rise due to consolidation effects associated with the loading. A similar effect is well-established for surface foundations and pipelines, and is allowed for in design practice (e.g. Gourvenec et al. 2014, 2020; Randolph &

Gourvenec, 2017; White & Bransby 2017). There is some support for the same mechanism to apply to plate anchors, based on model test results (e.g. Han et al. 2016; Zhou et al. 2020).

The purpose of this paper is to report a systematic numerical study into the capacity of plate anchors embedded in soft soils, and to identify the effect of sustained loading and consolidation on the anchor capacity. The numerical approach is first benchmarked against established solutions, then extended to explore consolidation-induced changes in capacity. The results quantify the potential capacity gain and show that these effects can be captured through simple analytical expressions, which can be used to represent the changing anchor capacity in a model of the mooring-anchor system behaviour.

1.2. Monotonic capacity of plate anchors

The monotonic capacity of plate anchors under undrained loading conditions has been well established in experimental model testing (Gaudin et al., 2006; Blake et al., 2010; O'Loughlin et al., 2014), field testing (Blake et al. 2015; O'Loughlin et al. 2016) as well as analytical and numerical modelling (Martin and Randolph 2001, 2003; Murff et al. 2005; Yang et al. 2010; Wang et al. 2014, 2009; Yu et al. 2015). These numerical studies have led to definitive solutions for the bearing

---

Nomenclature

Symbols

B	anchor breath or diameter
e	void ratio
f_{su}	scaling factor for gain in capacity
f'_{su}	incremental scaling factor for gain in capacity
G	gain in capacity $\frac{V_{cu}}{V_{uu}}$
H	anchor plate embedded depth
m_v	modulus of compressibility
N_c	bearing factor
p'	mean effective stress
P	preload level (V_p/V_{uu})
q	is deviatoric stress
q_p	preload stress
Q	bearing capacity of the foundation
s_u	undrained soil strength
s_{ui}	initial undrained soil strength
S	symmetry of the mechanism
T	dimensionless time factor
t	elapsed time since the start of consolidation

U	degree of consolidation
R	undrained strength ratio $\left(\frac{s_u}{\sigma'_{v0}}\right)_{NC}$
v	specific volume
V_{el}	volume of an element
V_p	static preload
V_{cu}	consolidated undrained vertical bearing capacity
V_{uu}	undrained uniaxial vertical bearing capacity
w	displacement of plate
z	depth coordinate in soil bed
Δz	distance from plate
α	factor to represent the proportion of the preload that acts below the plate
$\Delta \epsilon$	incremental shear strain
ϵ_p	plastic strain increment
γ	unit self weight
Γ	y-intercept at a mean effective stress of 1 kPa
σ'_{v0}	in situ effective vertical stress
λ	gradient of the critical state line
ν	poisson's ratio
ϕ_{cs}	critical state friction angle

---

capacity of plate anchors under undrained loading, where the bearing capacity, Q is linked to the soil undrained strength s_u via a bearing factor, $N_{c,deep}$:

$$Q = AN_{c,deep}s_u \qquad (1.1)$$

where A is the area of the plate. This expression applies if the anchor is buried sufficiently deep that the failure mechanism does not reach the soil surface, so there is no additional term associated with the overburden surcharge. The exact bearing factor for an infinitesimally thin circular (axisymmetric) plate, with soil bonded to the underside, is $N_{c,deep}$ = 13.11 (Martin and Randolph 2001).

However, there are two further effects on the undrained capacity that are relevant to long term sustained loading: (i) gap formation beneath the plate and (ii) changes in soil strength. Gap formation is explained further below, but refers to the process by which there is a loss of contact between the plate and soil beneath, with the resulting gap becoming filled with water through a seepage process.

If sufficient interface tension is available during uplift, then the soil above and below the plate is involved in the failure mechanism. Alternatively, the soil can separate from beneath the plate when the plate is pulled upward, resulting in a one-sided mechanism (Han et al. 2016; Maitra et al. 2019, 2022). Published solutions often assume either unlimited or zero tension is available. In reality, negative excess pore pressure develops below the plate when it is loaded upward (Maitra et al. 2019). Under sustained load, this sets up seepage flow towards the anchor base, driven by differences in pore pressure above and below the plate anchor relative to the far field. In such cases, for continuity, a gap filled with water must form beneath the plate anchor, with seepage of water into the gap. Previous numerical modelling of plate anchors has explored this effect by allowing a loss of plate-soil contact beneath the anchor when zero total stress is reached at this interface (Han et al. 2016). This assumption differs from a water-filled gap because it does not enforce continuity of volume to control the growth of the gap. Other studies have enforced volume continuity in their modelling of seepage and water-filled gap formation by introducing soft poro-elastic elements in numerical simulations of suction caissons (Cao, 2003), skirted foundations (Mana et al. 2014), and plate anchors (Maitra et al. 2019). The same approach is used in this study, and in addition, the effect of consolidation on soil strength is incorporated via the Cam clay soil model.

1.3. Consolidated capacity of foundations and anchors

The consolidation-induced increase in the undrained capacity of shallow and surface foundations resting on soft clay is well understood from field tests (Lehane et al. 2003; Gaone et al. 2018), centrifuge tests (Lehane et al. 2005; Vulpe et al. 2014) and numerical analyses (Zdravkovic et al. 2003; Gourvenec et al. 2014; Feng et al. 2015; Stanier et al. 2019; Liu et al., 2020; Yi et al., 2021). These increases in foundation capacity result from gains in soil strength during consolidation under a static preload or dead load. A simple linear relationship between preload level, soil undrained strength ratio and gain in capacity exists for soil following Cam clay-type behaviour, which leads to simple analytical design expressions for practical exploitation of these gains in capacity (Gourvenec et al. 2014). For clay that is initially normally-consolidated, with a typical undrained strength ratio, $R = \left(\frac{s_u}{\sigma'_{v0}}\right)_{NC}$ of 0.25, a static dead load equivalent to a factor of safety of two leads to a 40 % gain in foundation capacity from consolidation (using the expressions in Gourvenec et al. 2014).

These significant gains in capacity for surface foundations, which are predictable via a simple framework, motivate this study of the equivalent long-term capacity changes of embedded plate anchors. In this case the consolidation of the soil above and below the embedded plate is important (O'Loughlin et al. 2017; Chen et al., 2022). Recent centrifuge tests reported by Zhou et al. (2020) have shown gains in embedded plate anchor foundation capacity due to sustained preloading. Singh and Chatterjee (2018) reported numerical simulations of consolidation-induced changes in soil strength around embedded strip anchors subjected to preload, although the resulting effect on anchor capacity was not reported. Building on those previous studies, this paper provides a systematic study, including identification of the underlying mechanism of changing soil strength, to show the coupled soil-plate anchor interactions, the influence of gap formation, and the resulting gains in capacity.

1.4. Objectives

This study uses small strain finite-element analysis in PLAXIS 2D, a commercially available finite element software, with a modified Cam clay (MCC) critical state model, to investigate consolidation and strength gain around an embedded plate anchor under sustained
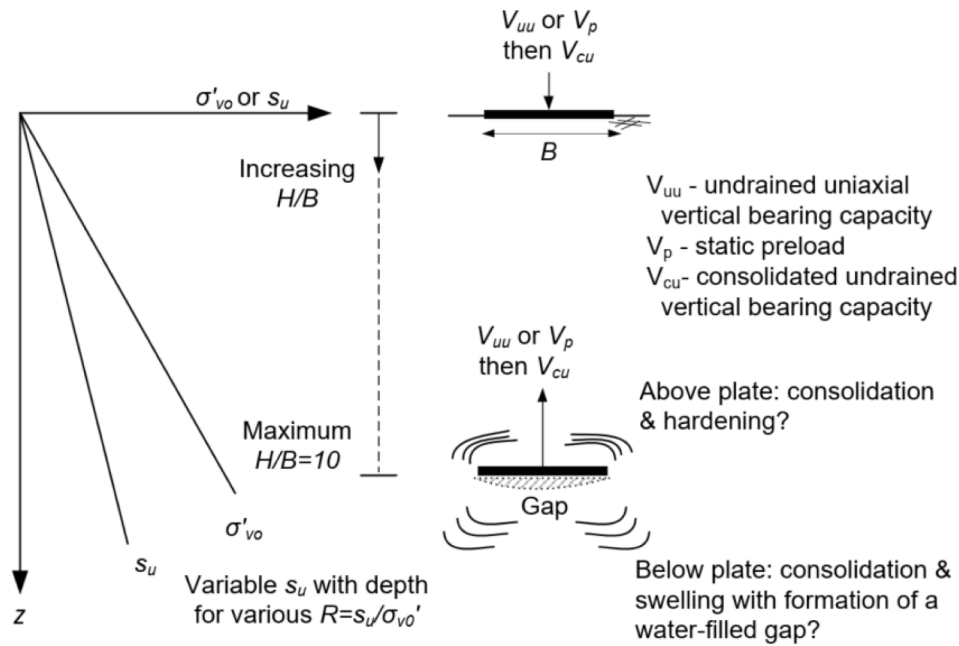
Fig. 1. Problem definition and study scope.

Table 1
Material Parameters.

Parameters adopted in finite-element analysis	Base case values	Modified case values
Elastic parameters		
Recompression index,κ	0.044	
Poisson ratio,ν	0.25	
Plasticity parameters		
Virgin compression index,λ	0.205	
Stress ratio at critical state,$M = q/p'$	0.89	0.445, 1.78
Derived parameter:$R = (s_u/\sigma_{vo}')_{NC}$	0.22 [a], 0.36[b],	0.12 [a], 0.39 [a]
Other parameters		
Effective unit weight, γ': kN/m^3	8	
Permeability, k: m/s	1.3×10^{-10}	

[a] axisymmetric conditions and [b] plane strain.

Table 2
Benchmarking solutions.

Case	Present analysis (PLAXIS 2D)	Benchmark	
		Value	Source
Surface strip	5.13	5.141	Martin (2003)
Surface circle	5.97	6.047	Martin (2003)
Embedded strip	12.38	11.425	Martin & Randolph (2001)
Embedded circle	13.31	13.13	Martin & Randolph (2001)

loading, to develop a simple analytical prediction framework. Initially, benchmarking was performed to confirm the accuracy of the model for fully undrained conditions relative to analytical solutions for surface and embedded footings without consolidation effects. Thereafter, the changes in anchor capacity, the associated soil-plate interactions, and changes in surrounding soil strength are investigated.

2. Finite Element Model

2.1. Model Properties

Rigid circular and strip surface foundations and plate anchors with

rough interfaces were considered, with the problem definition and notation shown in Fig. 1. All models had an anchor with breadth or diameter, B=5m, however, all results have been appropriately non-dimensionalised so the exact size is irrelevant. Soft, normally consolidated clay conditions were represented. The parameters describing the soil material, as modelled using modified Cam clay, are given in Table 1. These parameters are derived from element testing programmes on kaolin clay reported by Stewart (1992) and Acosta-Martinez et al. (2006), and the strength profile is typical of soft seabed conditions (Randolph et al., 2011). As discussed later, the results are normalised with respect to the soil strength, so the conclusions apply to more general range of conditions.(See Table 2.).

Axisymmetric and plane strain finite-element meshes were used to model the circular and strip foundations. Schematic diagrams of the mesh configuration and boundary constraints for the surface and a deeply embedded footing case ($H/B = 10$) are shown in Fig. 2 and example finite element meshes are given in Fig. 3. The mesh boundaries were sufficiently far from the foundation to ensure no influence on the foundation response. A similar mesh discretisation was adopted in the axisymmetric and plane strain models.

The meshes adopted in this study contained approximately 13,000 elements in the axisymmetric case and 10,000 elements in the plane strain case. The required mesh density was determined via a mesh sensitivity analysis. In this analysis, 9 meshes were trialled, ranging from 350 elements to 17,000 and 12,500 in axisymmetry and plane strain respectively. It was found that the fully undrained capacity was constant (within 1 %) for the largest five mesh densities. The second largest mesh density was adopted for the subsequent analyses.

The surface footing and embedded plate were both represented as a rigid plate element, composed of line elements. The soil was represented by 15-noded triangular elements which used fourth-order interpolation for displacements and their numerical integration involved twelve Gauss points.

2.2. Scope and loading methods

The unconsolidated, undrained uniaxial vertical bearing capacity, V_{uu}, was determined for the surface footing and embedded plate in the plane strain and axisymmetric cases as an initial benchmarking exercise to validate the modelling with the well-established, analytical solutions
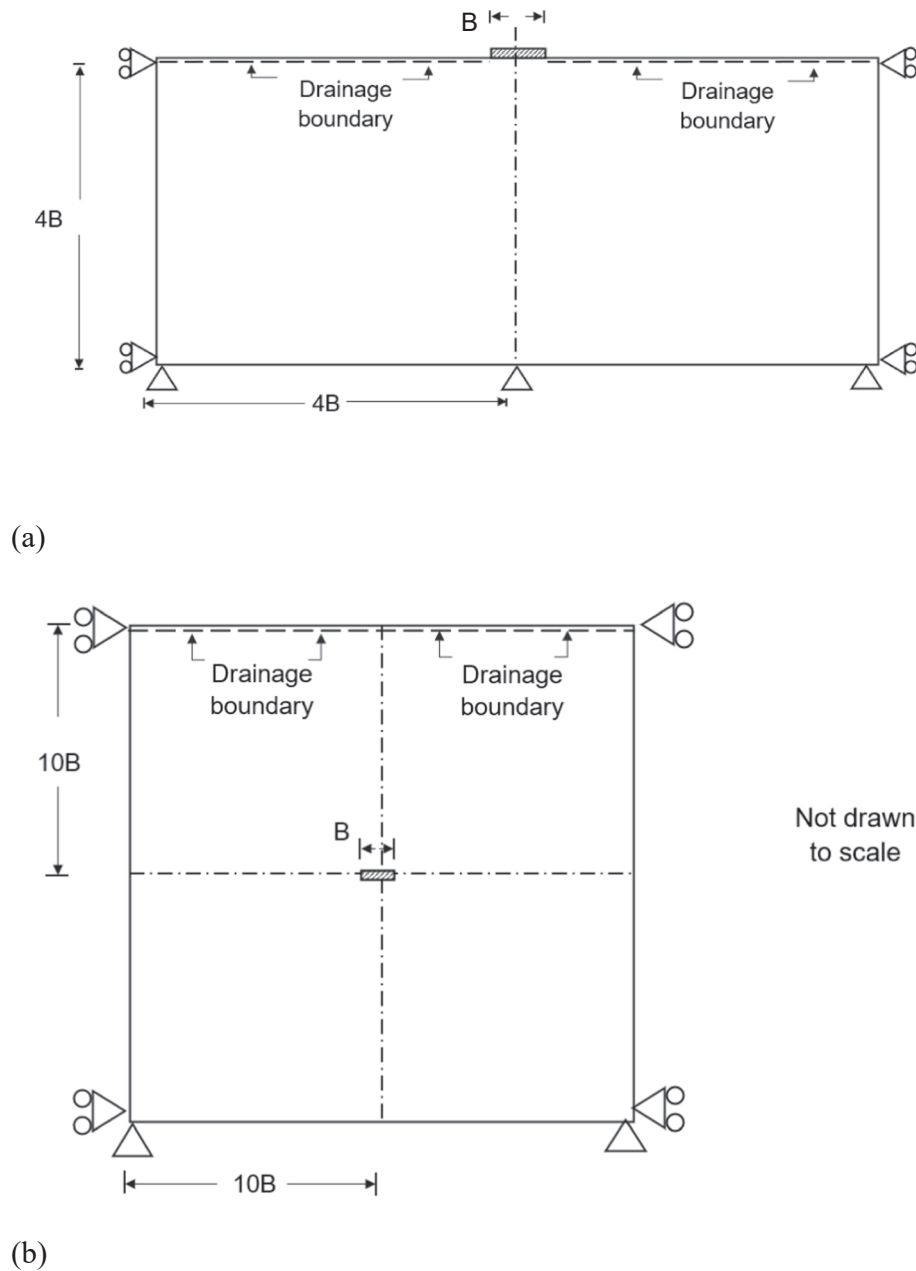
(a)

(b)

Fig. 2. Schematic diagram for the adopted mesh configurations in (a) surface footing and (b) embedded plate anchor cases.

described in Martin et al. (2001) and Martin (2003). Further benchmarking compared the gain in the capacity of the surface footings after allowing consolidation under a static preload V_p, defined as a proportion of V_{uu}. The subsequent consolidated undrained vertical bearing capacity, V_{cu}, was compared to results from Gourvenec et al. (2014). Once benchmarking was completed, the increase in consolidated capacity from static preloading of an embedded circular plate anchor was investigated.

Each analysis that included a consolidation phase involved the same principal steps:

(a) establishment of the in-situ effective stress conditions
(b) preloading the foundation with V_p
(c) a consolidation period, sufficient for full excess pore pressure dissipation (i.e. excess pore pressures reduced to a value $u < 0.1$ kPa)

(d) a vertical displacement of the foundation causing undrained vertical bearing failure, mobilising V_{cu}

The in-situ state of the soil was established by allowing the soil to reach equilibrium under the assigned unit self-weight, γ and an applied surface surcharge. A nominal surface surcharge of 10 kPa was applied to avoid a zero effective stress state at the mudline. A period of consolidation was then prescribed, for full dissipation of the surcharge-induced excess pore pressure to complete the establishment of the in-situ stress conditions.

In the next stage, preloading was prescribed, encompassing cases from $V_p/V_{uu} = 0.1$ to 0.65. A period of consolidation was then allowed, before the soil was brought to failure under displacement-controlled undrained vertical foundation displacement to identify V_{cu}. In all the applied consolidation stages, the default consolidation time increment was adopted, which was automatically calculated by PLAXIS 2D in accordance with the criterion proposed by Vermeer and Verruijt (1981).
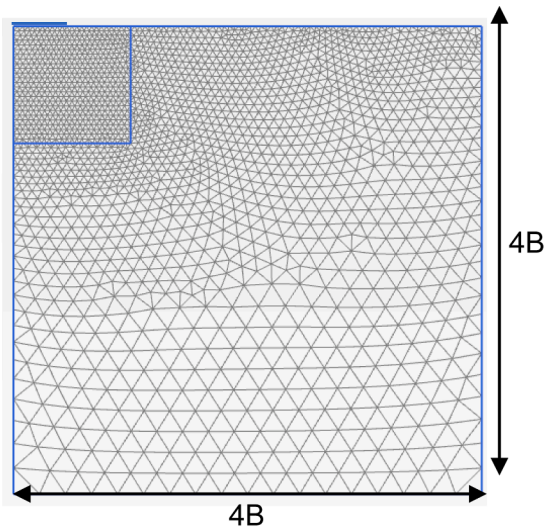
(a)
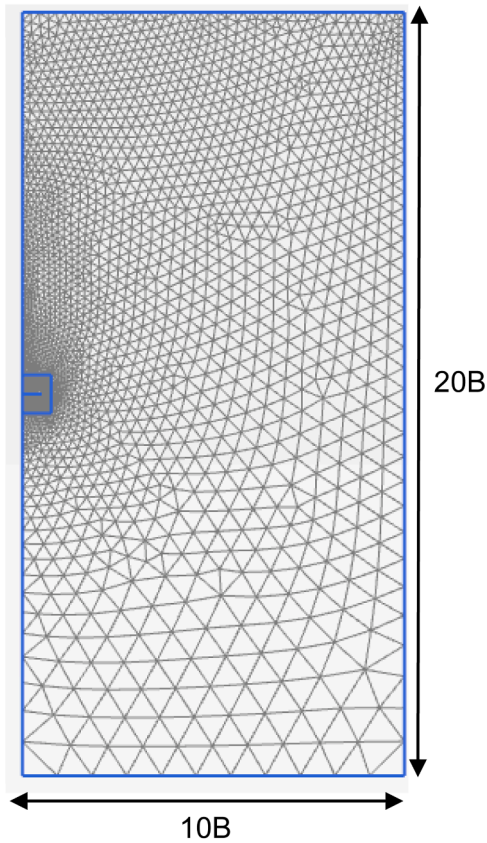
(b)

Fig. 3. Example of finite element mesh for (a) surface footing and (b) embedded plate cases.

2.3. Implementation of in situ strength profile

In PLAXIS 2D, although the model initialisation creates a linear increase in effective stress with depth, and therefore a linearly-increasing undrained shear strength, s_u, (when OCR is specified as 1), the initial void ratio, e_{ini} is set to be equal at all depths as a model input. Therefore, the critical state soil parameter representing the intercept, Γ, at a mean effective stress, p' of 1 kPa on the critical state line is a calculated parameter (not a model input), evaluated according to (Schofield et al. 1968):

$$\Gamma = v + \lambda \, ln\left(\frac{2s_u}{M}\right) \qquad (2.1)$$

The material parameter λ is the gradient of the critical state line, M is the stress ratio, q/p' at the critical state (where q is deviatoric stress), v is equal to $1 + e_{ini}$. This feature of the PLAXIS 2D Cam clay implementation has no effect on the model: the full soil bed is established in a normally-consolidated state and has the desired linear profiles of strength and effective stress.

The undrained strength initially varies linearly with depth such that in the axisymmetric case:

$$\frac{s_u}{\sigma'_{v0}} = \frac{sin\phi_{cs}}{2a}\left(\frac{a^2+1}{2}\right)^{\Lambda} \qquad (2.2)$$

where $\sigma'_{v0} = \gamma' z$. For the plane strain case, due to the use of the von Mises failure criterion:

$$\frac{s_u}{\sigma'_{v0}} = \left(\frac{2}{\sqrt{3}}\right)\frac{sin\phi_{cs}}{2a}\left(\frac{a^2+1}{2}\right)^{\Lambda} \qquad (2.3)$$

The material parameter ϕ_{cs} is the critical state friction angle and the constants a and Λ are defined according to:
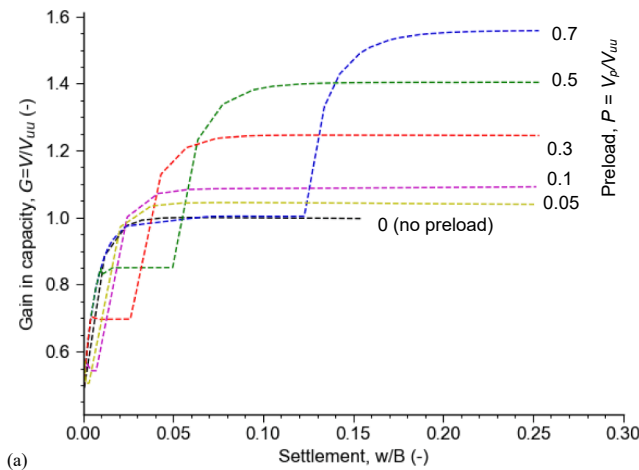
$$a = \frac{3 - sin\phi_{cs}}{2(3 - 2sin\phi_{cs})} \qquad (2.4a)$$

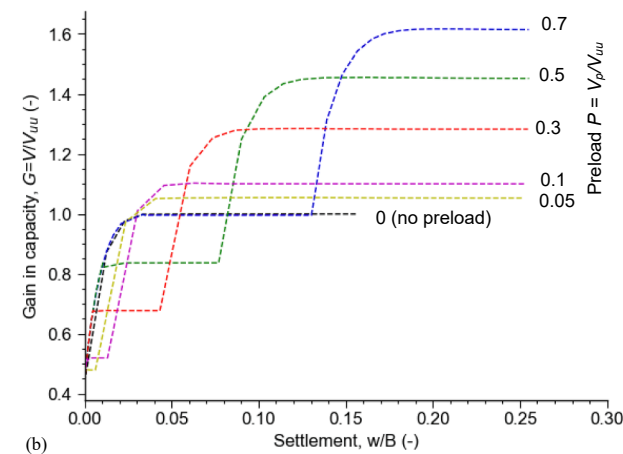$$\Lambda = \frac{\lambda - \kappa}{\lambda} \qquad (2.4b)$$

Once the model was initiated and the surcharge applied, it was confirmed that the strength profile was as predicted using the expressions above, with OCR = 1 at all depths. For subsequent assessment of s_u and mapping of the changes in strength, the void ratio throughout the model was used to calculate undrained strengths according to Equation (2.1) where $v = 1 + e$ and e is the current void ratio in each element in the simulation.

The adopted base case parameters led to a normally-consolidated undrained strength ratio $\left(\frac{s_u}{\sigma'_{v0}}\right)_{NC}$ of ~ 0.22 which is typical for soft clay.

Previous studies have modelled plate-soil separation and the formation of a water-filled gap by inserting soil elements with very low effective stiffness and strength where the gap will form, so that the water phase controls the volumetric stiffness and the shear strength is essentially zero (e.g. Mana et al. 2014). In this study, no such additional material nor constraints were needed due to the asymptotic volumetric behaviour of Cam clay at low effective stress. The volumetric stiffness of the soil skeleton and the shear strength both diminish towards zero with reducing effective stress in the Cam clay model. Consequently, the stiffness and the strength of the material become controlled by the properties of the pore water phase. The Cam clay elements therefore faithfully represent a water-filled gap automatically if the applied total stress and the consolidation process cause the effective stress to diminish to zero at any location in the model. This eliminates the need to introduce low stiffness elements at pre-determined locations where a gap is expected to form. Instead, a water-filled gap forms naturally, controlled by seepage flow, at any appropriate location.

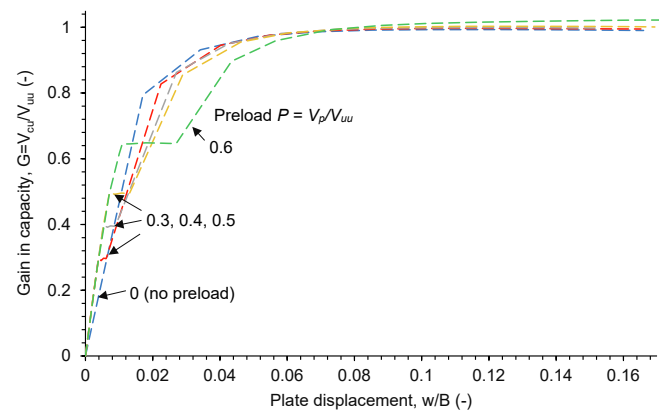Fig. 6. Normalised load-settlement profiles for embedded rough circular plates.

(2003). For the embedded plate, ultimate bearing capacity factors of N_c = 13.13, and 12.38 were obtained for the axisymmetric and plane strain embedded footing cases respectively, which are within 1 % and 8 % respectively of the exact solutions presented in Martin et al. (2001). These results confirm that the numerical simulation was accurate for undrained collapse calculations and the minor discrepancies were comparable to other studies (e.g. Gourvenec et al., 2003a,b).

3.2. Consolidated undrained capacity of surface foundation

The effect of consolidation under a static preload in the range V_p/V_{uu} from 0.05 to 0.7, on the consolidated undrained vertical bearing capacity, V_{cu}, was also used as a benchmark case in PLAXIS 2D. The governing equations of consolidation used in PLAXIS are based on Biot's theory for coupled consolidation (Biot, 1956). Fig. 4a and b show the gain in bearing capacity, via the changing vertical load-settlement responses. Fig. 5 summarises these observed gains in bearing capacity, compared to prior results from Gourvenec et al. (2014). The gains in capacity from the present study are proportional to the preload level, matching the relationship set out by Gourvenec et al. (2014):

$$G = 1 + RN_c f_{su} P \qquad (3.1)$$

where G represents the gain in capacity (V_{cu}/V_{uu}), R is the strength ratio $\left(\frac{s_u}{\sigma'_{v0}}\right)_{NC}$ following Wroth (1984), f_{su} is the scaling factor from Gourvenec et al. (2014) and P is the preload level (V_p/V_{uu}). The fitted values of f_{su} are within 5 % of those calculated in Gourvenec et al. (2014), indicating that the effect of consolidation is successfully benchmarked against prior work. The typical value of $f_{su} = 0.45$ means that for the base case soil parameters, a sustained preload of V_p leads to a gain in capacity of ~ 0.8 V_p through consolidation (because $RN_c f_{su} \sim 0.8$).
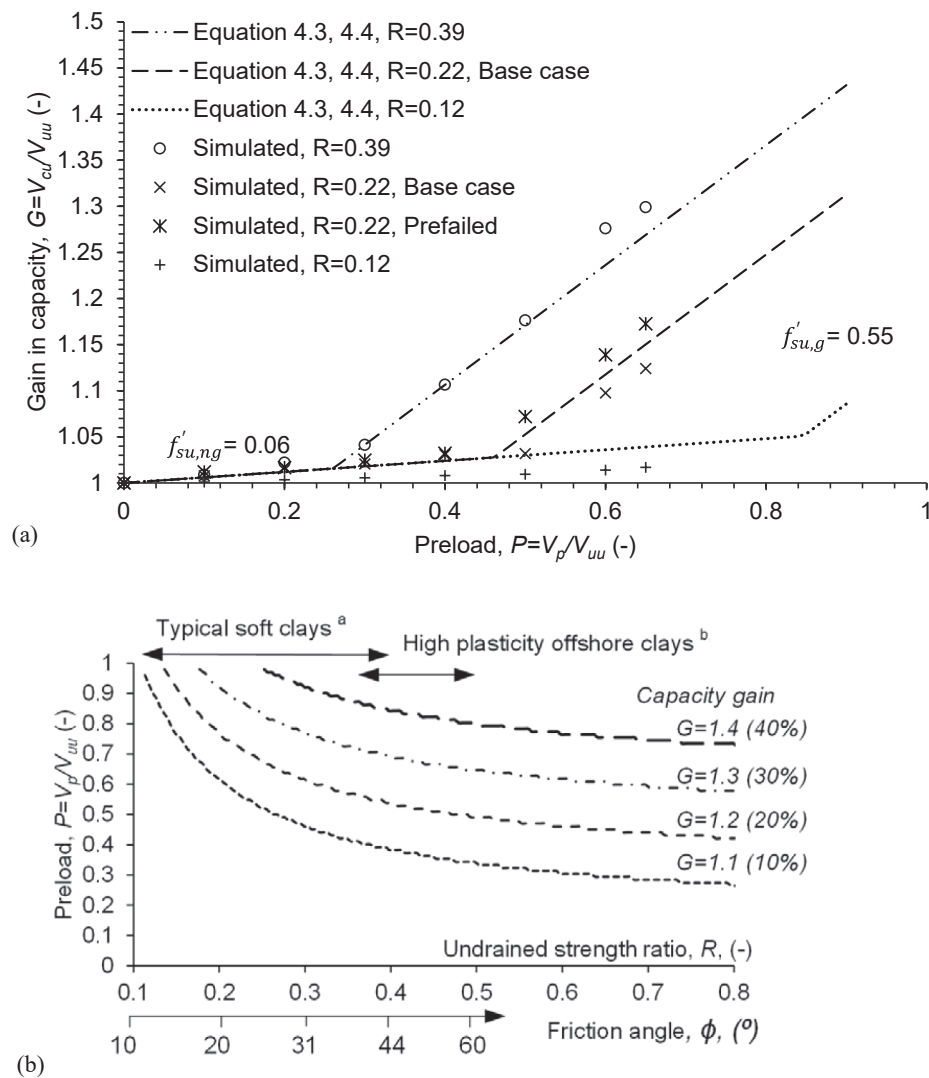
4. Consolidated Capacity of Embedded Plates

4.1. Gains in capacity from preloading

The gains in consolidated capacity for the embedded circular plate varied non-linearly with preload level and were lower compared to the surface footing case (Figs. 6 and 7). There are two distinct regions of response. At low loads the best fit scaling factor is $f_{su} = 0.06$. At higher preload above a threshold of $P \sim 0.4$ to 0.5, the gain is more significant and has a best fit higher scaling factor of 0.55. These scaling factors can be indicated by an *incremental* scaling factor, denoted f'_{su}, by differentiating Equation (4.1):

$$\frac{dG}{dP} = RN_{c,deep} f'_{su} \qquad (4.1)$$

The bi-linear gains in capacity are caused by changing soil-plate

Fig. 4. Normalised load-settlement profiles for rough surface (a) circular and (b) strip footings.

Fig. 5. Benchmarking of effect of consolidation on bearing capacity of surface foundations.

3. Benchmarking Results

3.1. Undrained capacity without consolidation

For the surface foundations, the unconsolidated undrained vertical bearing capacity V_{uu} was within 2.5 % of the analytical predictions determined using the method of characteristics, as defined in Martin

Fig. 7. (a) Normalised gains in bearing capacity, G after consolidation under normalised preload, P for deeply-embedded circular plates and a range of strength ratio, R; (b) Contours of predicted gains in bearing capacity, G for variable undrained strength ratio, R, or friction angle, ϕ and preloads, P.

anchor interactions above and below a preload threshold. During sustained upward loading, the soil above the plate compresses and strengthens, while soil below the plate is unloaded. The threshold occurs where a gap forms, caused by the applied preload being sufficient to reduce the effective stress beneath the plate to zero. After this gap forms during the consolidation phase, a higher proportion of the preload is resisted by the soil above the plate. Therefore, the soil above the plate experiences a higher compressive stress as a proportion of the preload stress, leading to greater densification and gain in strength, yielding a greater gain in subsequent capacity. The two scaling factors are therefore denoted $f'_{su,ng}$ and $f'_{su,g}$, corresponding to no-gap (low P) and with-gap (high P) conditions.

The undrained strength ratio, R also affects the influence of preloading on anchor capacity. This soil parameter was varied, with $R = 0.12$, 0.22 and 0.39, to investigate its effect on the threshold associated with gap formation and the transition in f'_{su} from $f'_{su,ng}$ to $f'_{su,g}$ as also shown in Fig. 7. The variation in R was achieved by changing the strength parameter M (see Table 1). The range 0.12–0.39 spans the typical range for natural clays. For example, Wood (1990) presents collated data of R as a function of plastic index, I_p, showing a general trend of R rising with I_p from 0.15 to 0.45, with a few scattered points

having even higher strength ratios. More recent studies of offshore soft clays show examples of very high values of R, such as the Colliat et al. (2010) review of West African offshore soft clays which show $R \sim 0.4$–0.5, due to the combination of very high moisture content (and therefore low unit weight) and high friction angle.

An increase in R resulted in greater gains in capacity once a gap formed beneath the plate. The preload required for gap formation, P_{gap}, is lower for higher R, because the soil strength is higher relative to the in situ vertical effective stress. Once the preload exceeds P_{gap}, further increments of preload are fully carried as compression in the soil above the plate. Using this observation, R can be linked to P_{gap}, to provide a simple extension of Equation (3.1) to predict the gains in capacity, as described below.

4.2. Analytical expressions for capacity gain

Based on the above analyses, the capacity gain from consolidation depends on whether a gap forms beneath the plate. Without a gap, the low 'no gap' gain parameter $f'_{su,ng} = 0.06$ applies, but once a gap forms this parameter rises to $f'_{su,g} = 0.55$, which is comparable to the response observed for surface foundations. The analyses show that two factors
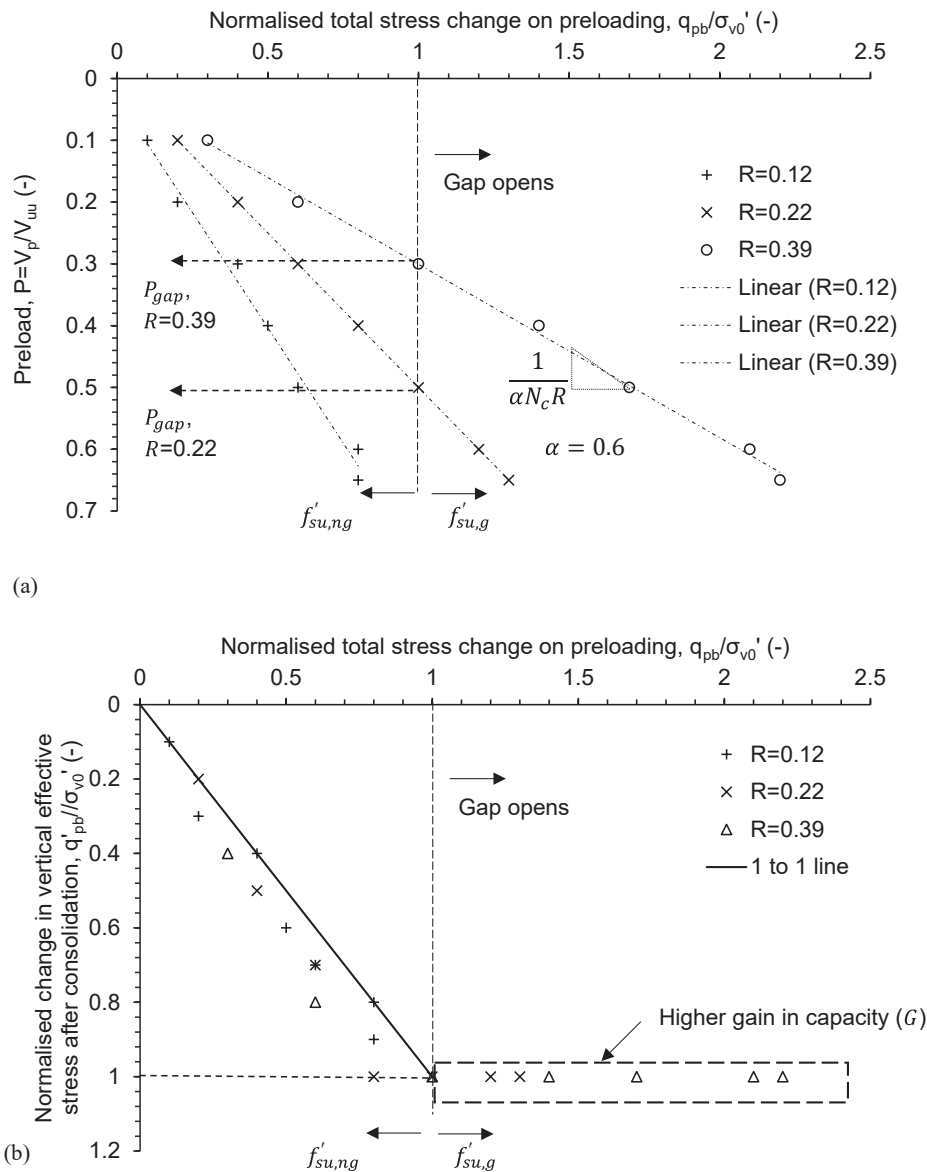
(a)

(b)

Fig. 8. (a) Effect of strength ratio, *R* and preload *P* on gap formation and (b) the corresponding relationships between applied total stress and resulting effective stress beneath the plate.

affect this transition behaviour:

(a) The preload stress, $q_p = V_p/A = PN_c s_u$ relative to the in situ vertical effective stress, σ'_{vo}

(b) A load-sharing factor α to represent the proportion of q_p that acts below the plate

Two preload-induced stress changes beneath the plate can be used to examine this transition: (i) the immediate vertical total stress change on preloading (denoted q_{pb}, and shown on Fig. 8a and b), and (ii) the effective vertical stress change after consolidation (denoted q'_{pb} and shown on Fig. 8b).

A gap forms if $q_{pb} > \sigma'_{vo}$, because the effective stress under the plate falls to zero. For normally-consolidated soil, this condition leads to a preload threshold for gap formation of:

$$P_{gap} = \frac{1}{\alpha N_{c,deep} R} \tag{4.2}$$

The total stress load sharing factor, $\alpha = q_{pb}/q_p$ is consistently ~ 0.6 (see Fig. 8a) for all preload levels and *R* values. Increasing the applied preload gives proportionate increases in the total stress change beneath the plate. Further simulations using a range of λ/κ ratios showed that α is also insensitive to this stiffness ratio.

The effective stress load sharing factor $\alpha' = q'_{pb}/q_p$ varies when a gap opens, because q'_{pb} is limited by a maximum of σ'_{vo}. This transition is shown in Fig. 8b, and once the gap opens, the results also show a higher gain in capacity. There is a small difference between q'_{pb} and q_{pb}; the immediate decrease in total stress was slightly larger than the final change in effective stress (i.e. the no-gap results lie below the parity line in Fig. 8b). This is because the top and bottom soil-plate interactions are not purely oedometric, and are also not completely separable, but rather form part of the soil mechanism that flows around the plate when loads are applied. These stress changes also do not necessarily map directly to changes in soil strength and capacity. Therefore, a modified fitting parameter α^* is used to translate Equation (3.1) into a capacity prediction expression:
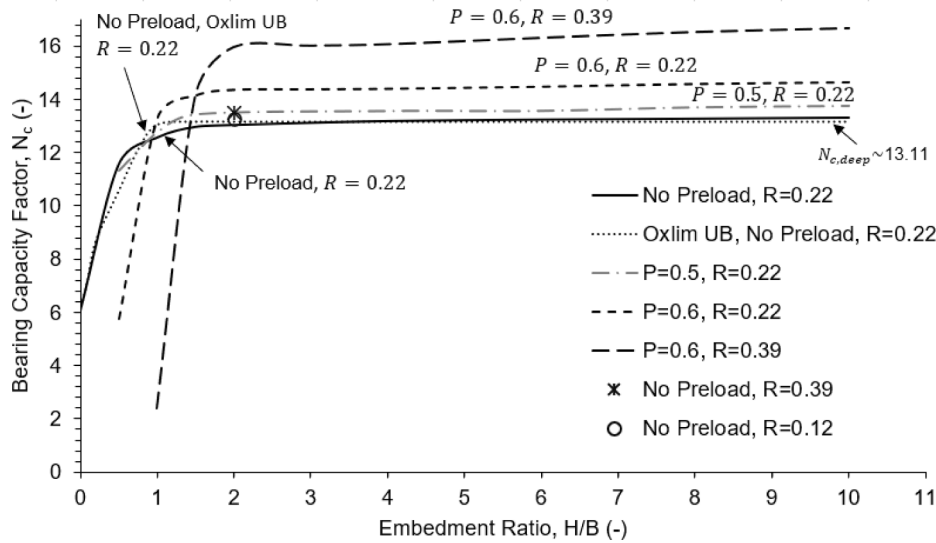
Fig. 9. Influence of embedment depth on bearing capacity factor, N_c (circular plate).

$$G = 1 + RN_{c\_deep}\left(f'_{su,ng}P + \left(f'_{su,g} - f'_{su,ng}\right)\left[P - P_{gap}\right]\right) \qquad (4.3)$$

where [ ] represents Macauley brackets, $f'_{su,ng} = 0.06$, $f'_{su.g} = 0.65$ and

$$P_{gap} = \frac{1}{\alpha^* N_c, deepR} \qquad (4.4)$$

with $\alpha^* = 0.75$.

Using this expression, the transition between the low-gain symmetric consolidation mechanism and the high-gain asymmetric mechanism can be predicted. The calculated gain in capacity is always within 3 % of the numerical results, as shown in Fig. 7a. Equation (4.3) can also be used to find the sustained preloads required to achieve a targeted gain in capacity within soft clays of different undrained strength ratios, R (or friction angles, ϕ) as shown in Fig. 7b. The undrained strength ratio R, and friction angle, ϕ are related based on the expression below (Wroth, 1984).

$$R = \sin(\phi)\left(\frac{1}{2}\right)^{\Lambda} \qquad (4.5)$$

where typical values of $\Lambda \sim 0.8$ for clay have been used to generate the gain in capacity contours plotted in Fig. 7b.

4.3. Effect of plate embedment ratio

A further range of simulations were performed for varying plate embedment ratio, H/B, from zero to 10, to identify the variation in bearing factor, N_c with plate depth, with and without preloading and consolidation. The limiting 'deep' bearing factor of $N_{c,deep} \sim 13.11$, associated with a failure mechanism that does not breach the soil surface, is achieved at all embedments greater than $H/B \sim 2$ for the adopted range of R (Fig. 9). The monotonic unconsolidated capacities from the PLAXIS 2D simulations were consistent with results from Oxlim, a numerical program which uses finite element limit analyses (FELA) to find bearing capacity solutions (Makrodimopoulos et al., 2007).

Only two diameters of embedment are required to mobilise the 'deep' bearing due to the compact shape of the failure mechanism mobilised in the soil around embedded circular plates. For preloaded cases, where the deep mechanism is mobilised, the same gain in capacity is observed for all H/B (Fig. 9). With reducing embedment, the capacity gain also reduces, until the plate capacity falls as a result of the preloading process. This reflects a situation in which the strength gain in the diminishing volume of soil compressed above the plate is eclipsed by the strength reduction in the volume of soil beneath the plate that is subjected to tension and swelling.

These results show that in normally-consolidated clay, the embedment required to mobilise the full 'deep' bearing capacity factor is relatively small, which is in contrast to previously published results showing the variation in N_c with H/B for strip anchors embedded in soil with uniform strength (e.g. Merifield et al. 2001, 2003; Nguyen and Merifield, 2012; Singh et al. 2017) and for circular anchors embedded in soil with varying cohesion with depth (e.g. Khatri et al. 2009; Bhatta-charya et al. 2015,2016). Studies for uniform soil typically model a higher ratio of undrained strength to geostatic vertical stress, so a failure mechanism involving vertical shear planes to the surface is more favourable than in this study. For strip foundations, the 'deep' failure mechanism has a greater vertical extent (Martin et al. 2001), and so the plate must be buried more deeply to prevent the failure mechanism reaching the soil surface.

In summary, Fig. 9 shows that the conclusions throughout this paper based on the deeply embedded case ($H/B = 10$) are generally applicable to all embedments $H/B > 2$ for linear strength profiles across the realistic range of strength ratio, R. It is not necessary for plate anchors to be more deeply buried to mobilise their maximum bearing factor, N_c, but naturally, the capacity of the anchor increases proportionally to the embedded depth due to the gradient of s_u.

4.4. Mobilised undrained strength around a deeply embedded plate

Prior to a gap forming beneath the plate, the consolidation process around deeply embedded plates, where the failure mechanism does not extend to the seabed surface, can be termed as symmetric with approximately equal but opposite changes in total stress, and subsequently effective stress, above and below the plate. Once a gap opens, the process can be termed asymmetric. The transition in the mobilised strength following symmetric and asymmetric consolidation processes can be quantified by calculating the volume-averaged mobilised undrained strengths $\overline{s_{u,mob}}$ of the failing soil in the regions above and below the plate as V_{cu} is mobilised. Following Stanier and White (2019), this mobilised strength is defined as:

$$\overline{s_{u,mob}} = \frac{\left(\int_{vol}\Delta\epsilon_p s_u \, dv\right)}{\int_{vol}\Delta\epsilon_p \, dv} \qquad (4.6)$$

where $\Delta\epsilon_p$ is the plastic shear strain during the final increment of the loading stage when V_{cu} is mobilised, s_u refers to the current undrained
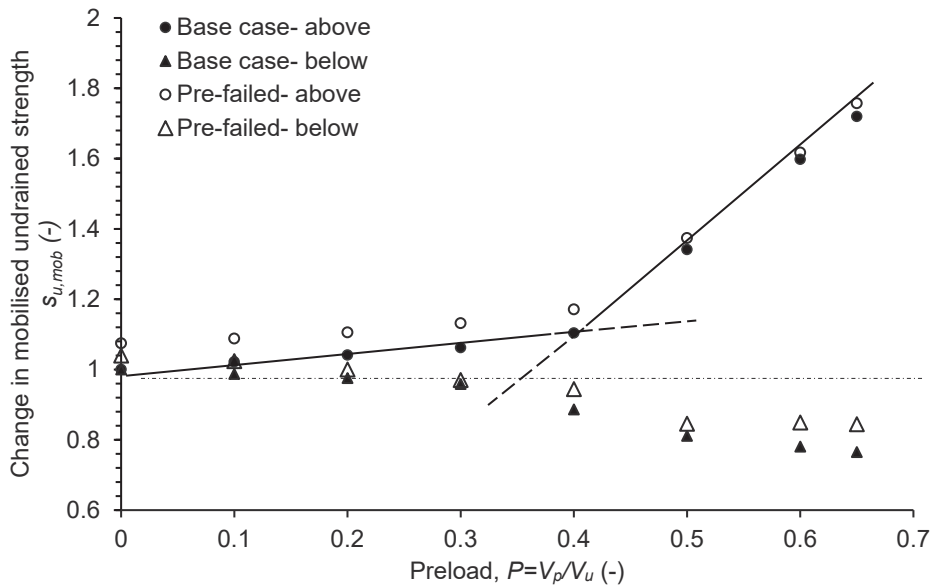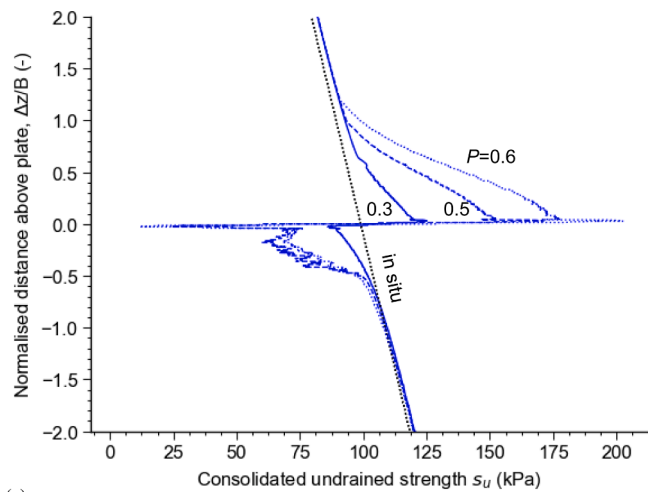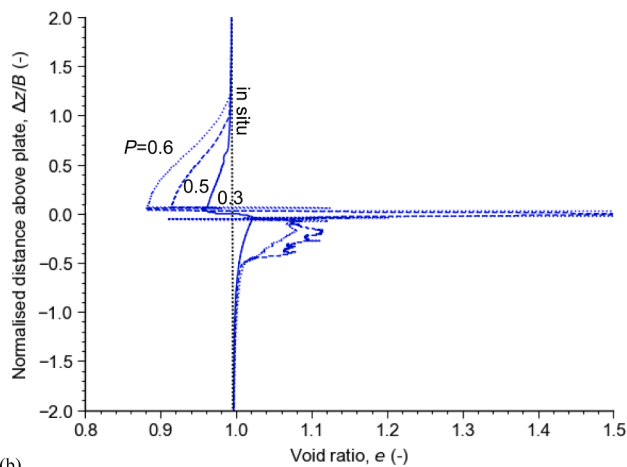
Fig. 10. Average mobilised undrained strengths in the regions of soil failure above and below a deeply embedded circular plate anchor after consolidation under preload, *P* in soil profiles with $R = 0.22$.

(a)

(b)

Fig. 11. Comparison of (a) undrained strength and (b) void ratio profiles at failure along the centre line in simulations where preloads of $P = 0.3$, 0.5 and 0.6 have been applied in soil profiles with R = 0.22.

strength of each element of soil within the deformation mechanism, and *dv* is the element volume. The integration is performed over the volume of the analysis domain either above or below the plate. Away from the plate, where there is no plastic deformation, $\Delta\epsilon_p = 0$, so these regions make no contribution to $\overline{s_{u,mob}}$.

Fig. 10 summarises these average undrained strengths in the soil regions above and below the plate for the case of $R = 0.22$. These average mobilised strengths have been normalised by the average mobilised strength when V_{uu} is mobilised. The average mobilised strength in the soil region above the plate increased more significantly for $P > 0.4$, reaching a gain in capacity of 70 % for $P = 0.65$. In the soil region below the plate, the mobilised strength decreased by an amount roughly proportional to *P* for the full range of preload, reaching a fall of 25 % at $P = 0.65$. In combination, these changes in mobilised strength account for the higher $f'_{su.g}$ for $P > 0.4$, albeit only resulting in a gain of 13 % in V_{cu} for $P = 0.65$. Similar trends but higher changes in strength were found for higher *R*.

The development of the different symmetric and asymmetric consolidation mechanisms is also evident when inspecting the element scale strength and void ratio behaviour, the average vertical total and effective stresses, and the effective stress paths in the soil regions above and below the plate, which are discussed in the following sections.

4.5. Changes in strength and void ratio from consolidation
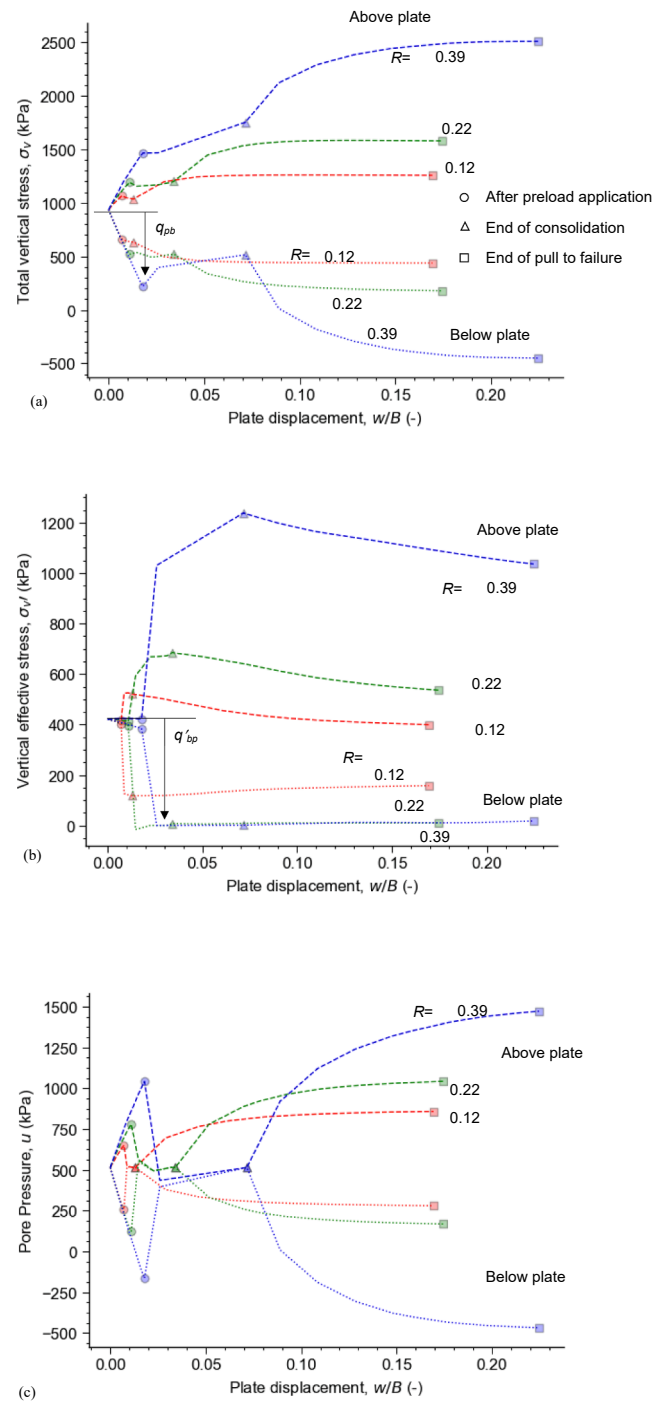
Fig. 11a and b compare the final undrained strength and void ratio profiles above and below the plate centreline, for different preload values. The soil above the plate strengthened under the preload, leading to a decrease in void ratio. Conversely, there was a decrease in strength and swelling below the plate. The increase in strength above the plate was slightly higher than the decrease in strength below the plate, consistent with the trends observed in Fig. 10.

For the highest preload level, a large increase in voids ratio is evident immediately below the plate, and a corresponding fall in s_u towards zero. This response reflects the influence of effective stress on compressibility in the MCC model: the stiffness of the soil skeleton is proportional to the effective stress. As a result, the voids ratio immediately below the plate can increase significantly, constrained only by the time required for inflow of water. In this respect, the MCC model produces the same effect as adding a thin layer of low stiffness elastic elements in regions where a water-filled gap can form, as used by other

10
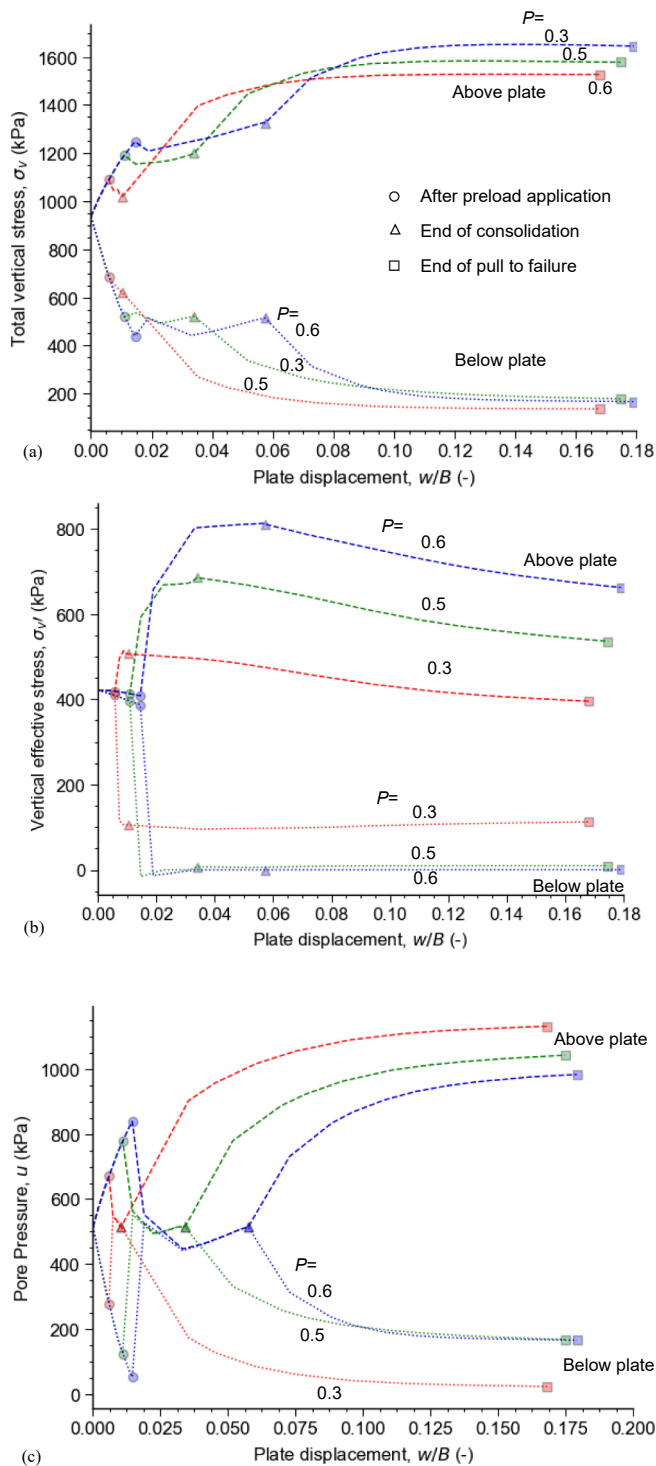
Fig. 12. Effect of preload on average (a) total stress and (b) effective stress (c) pore water pressure in the soil above and below the plate in soil profiles with R = 0.22.

Fig. 13. Effect of soil strength ratio, R, on average (a) total stress and (b) effective stress (c) pore water pressure above and below the plate for preload. $P = 0.5$

authors previously (e.g. Cao et al. 2003; Mana et al. 2014; Maitra et al. 2019). The region of high voids ratio and minimal s_u immediately below the plate is a proxy for a water-filled gap. The gap forms in a manner that respects volume continuity because the element can only enlarge following flow of pore water from the adjacent elements. This contrasts with some previous numerical studies of gap formation beneath plate anchors, which have allowed a gap to expand without imposing volume continuity, instead of only applying an equal pore pressure around the

internal surface of the gap. In this respect, the present study provides a simple but more rigorous method of simulating gap formation via the proxy of the volumetric response of MCC.

The additional gain in strength that occurs once a gap can form beneath the plate is evident in Fig. 11a. The doubling of P from 0.3 to 0.6 causes a tripling in the gain in s_u immediately above the anchor from 25 kPa to 75 kPa.

4.6. Average vertical total and effective stresses above and below plates

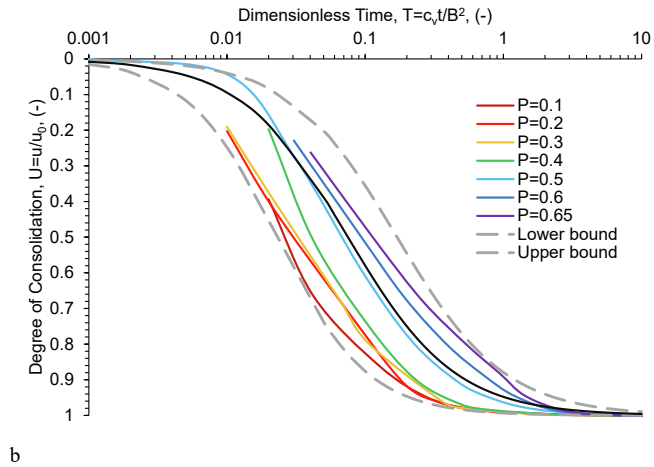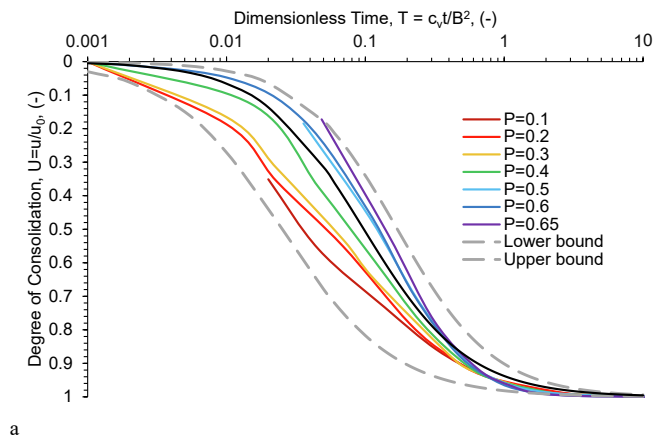The average vertical total and effective stresses that developed above

a

b

Fig. 14. Normalised time-dissipation of pore water pressure consolidation response (a) above and (b) below a deeply embedded circular plate ($z/B = 10$) for a range of preloads in soil profiles with R = 0.22.

Table 3
Values of T_{50} and constant m for fits to normalised time-excess pore water pressure dissipation response above and below deeply embedded plate (Equation (4.7)).

	Position relative to plate	T_{50}	m
Average	Above	0.098	1.165
	Below	0.08	1.12
Upper bound	Above	0.17	1.25
	Below	0.17	1.08
Lower bound	Above	0.023	1.33
	Below	0.025	1.12

and below the plate are shown in Fig. 12a and b for applied preloads of P = 0.3, 0.5 and 0.6. When the preload is applied, there is a greater change in vertical stress below the plate than above, showing that initially a majority of the load is resisted by a tensile increment beneath the plate rather than compression above. This load sharing reflects that the normally-consolidated soil has a higher stiffness when subjected to an unloading increment compared to the lower stiffness on virgin loading. If the vertical effective stress beneath the plate decreases to zero during the consolidation process (as is evident in Fig. 12b for P = 0.5 and 0.6), a gap filled with water (i.e. MCC with higher water content and negligible strength and stiffness) opens beneath the plate and a one-way consolidation mechanism forms. Subsequent loads are transferred as compression into the soil region above the plate, causing high increases in consolidated undrained strength and gains in plate pull out capacity. This change between a two and one-way consolidation mechanism occurs between preloads P = 0.3 and 0.5, which is consistent with the
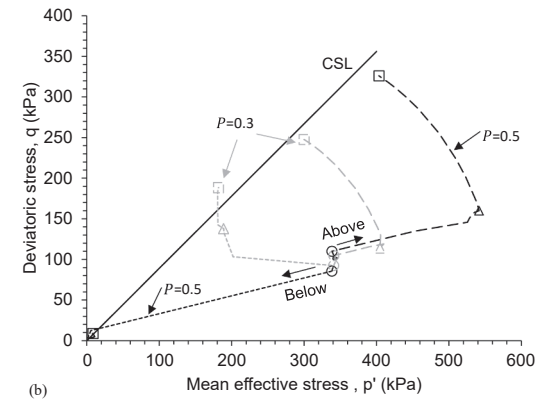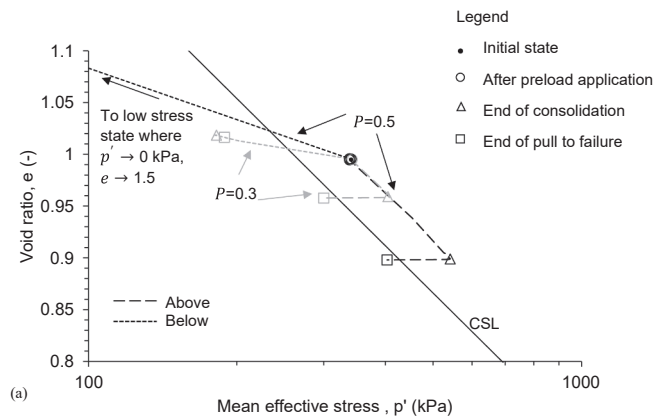

Fig. 15. Effective stress paths of elements located above and below, the plate in simulations with preload fractions of $P = 0.3$ and $P = 0.5$ in the (a) void ratio, e vs mean effective stress, p' and (b) deviatoric q vs p' spaces for soil profiles where R = 0.22.
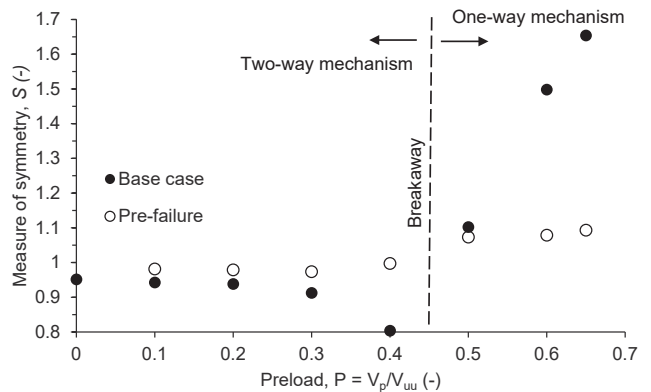

Fig. 16. Change in symmetry in the deformation in the soil above and below the plate involved in the failure mechanism for R = 0.22.

transition point in the strength and capacity gains for $R = 0.22$ observed in Figs. 7 and 10.

Varying the undrained strength ratio, R, in the analyses changes how the averaged total and effective vertical stresses are shared in the regions above and below the plate. For higher R, the in-situ soil strengths are higher relative to the vertical effective stresses and so the preload required for gap formation, P_{gap}, decreases. This trend is evident in Fig. 13, which shows the changing average stresses above and below the plate for $P = 0.5$ and the range of R. Initially, as the preload is applied, there is a slightly greater fall in total stress under the plate, compared to the gain in total stress above the plate. However, as these changes in
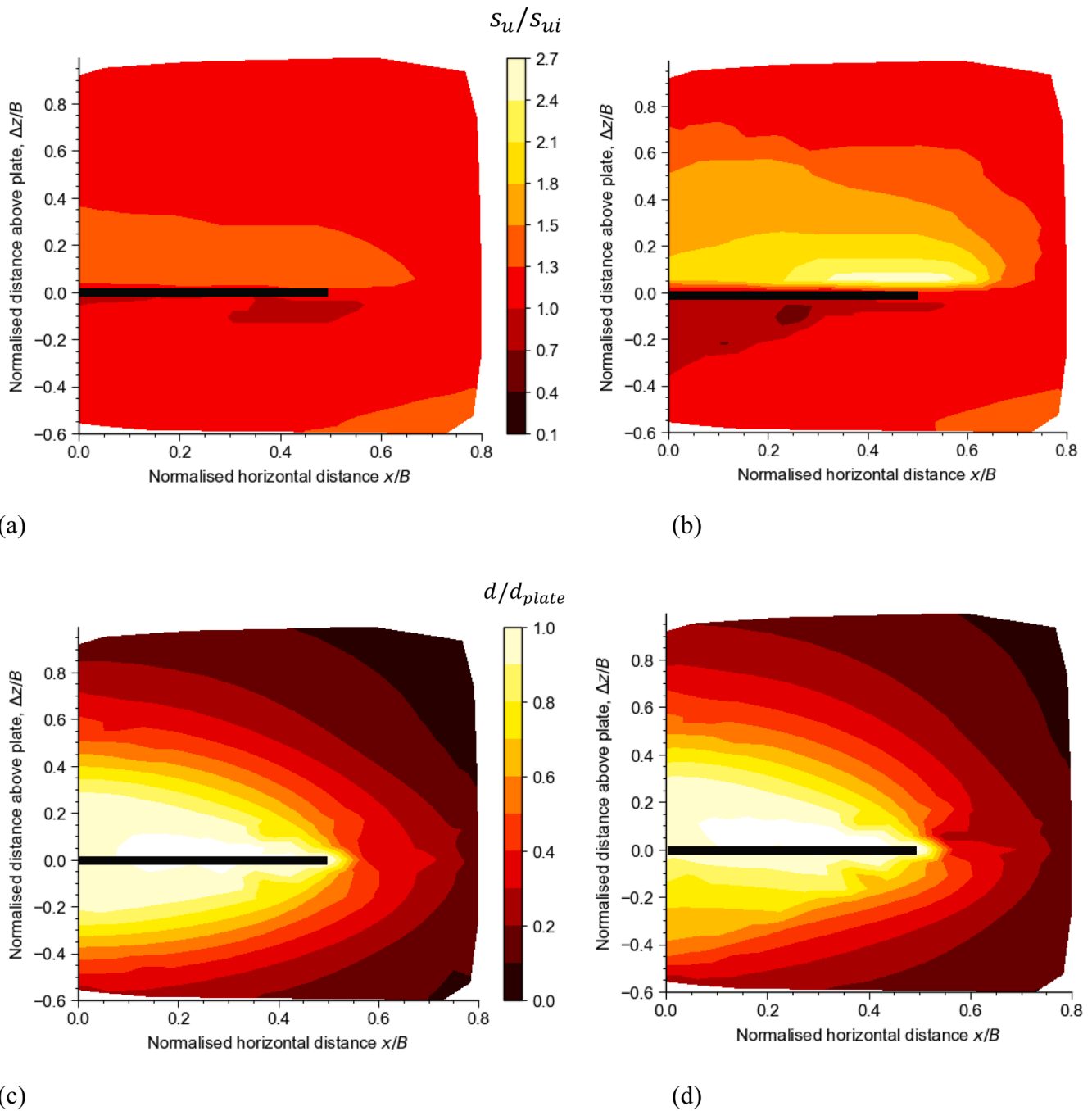
Fig. 17. Comparison of failure mechanisms for different preloads ($R = 0.22$): Strength contours for (a) $P = 0.4$ and (b) $P = 0.6$; Displacement zones for (c) $P = 0.4$ and (d) $P = 0.6$.

total stress convert to changes in effective stress during the consolidation process, gap formation occurs for $R = 0.22$ and 0.39, due to the effective stress failing to zero. When this occurs, a greater proportion of the applied preload is carried by an increase in effective stress above the plate once consolidation is complete.

4.7. Time-dissipation of excess pore water pressure histories

To utilise the gains in capacity described earlier for design purposes, it is necessary to quantify the time required for consolidation to occur after the preload is applied. For buried plates, the results can be normalised using methods described in Gourvenec et al. (2014) and Singh et al. (2018). Time is represented by the dimensionless time factor

$$T_v = \frac{c_v t}{B^2} \tag{4.7}$$

where c_v is a representative value of the coefficient of consolidation and t is the elapsed time since the start of consolidation. The coefficient of consolidation is defined as

$$c_v = \frac{k}{m_v \gamma_w} \tag{4.8}$$

where k is the soil permeability, γ_w is the unit weight of water (9.81 k N/m³) and m_v is the modulus of compressibility given by
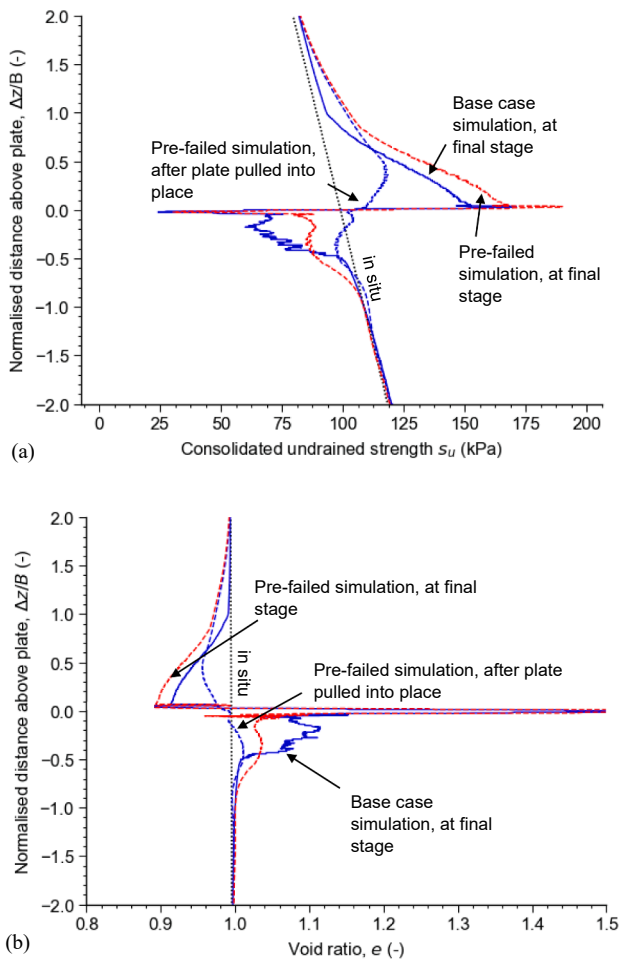
(a)

(b)

Fig. 18. Comparison between typical (a) undrained strength and (b) void ratio profiles at the centreline for base case and pre-failed simulations for preloads P = 0.5 for R = 0.22.

$$m_v = \frac{\lambda}{(1+e)\sigma'_{v0}} \tag{4.9}$$

based on the in-situ vertical effective stress, σ'_{v0}, and initial void ratio, e. The degree of consolidation is defined by the normalised excess pore water pressure dissipation response, $U = \frac{u}{u_0}$, considering the excess pore pressure, u, at points above and below the centre of the plate, relative to the initial value when the preload is applied, u_0. The normalised excess pore water pressure dissipation response above and below the plate is shown in Fig. 14 and can be approximated by a simple function:

$$U = \frac{1}{1 + \left(\frac{T}{T_{50}}\right)^m} \tag{4.10}$$

where T_{50} is the dimensionless time factor for 50 % of the consolidation to occur (i.e. $U = \frac{u}{u_0} = 0.5$) and m is a constant. Values of T_{50} and the constant m that best fit the bands of finite-element results, when the time factor is calculated in terms of the coefficient of consolidation are summarised in Table 3, and can be used to approximate the time required for generated excess pore water pressures to dissipate and gains in strength to occur post preloading. The values for T_{50} for the deeply embedded circular plate in this study were generally lower than the results for deeply embedded strip anchors ($z/B = 5$) in Singh et al. (2018). This is because the drainage path is shorter around circular plates than strip anchors and therefore, pore water pressures generated during the preloading dissipate more quickly. The average T_{50} of ~ 0.09

(Table 3) agrees with the solution for a circular surface plate on elastic soil of $T_{50} \sim 0.12$ given by Gourvenec et al. (2010). This is to be expected since the deeply buried plate has geometry and boundary conditions comparable to two surface plates positioned back-to-back.

The results show a variation in T_{50} for different preload levels (Table 3), which does not emerge from the elastic solution. This range reflects the different stiffnesses involved for different preloads, including the lower stiffness associated with a fall in effective stress leading to gap formation. The tabulated values of T_m and m can be used to approximate the time required to dissipate the excess pore pressures and achieve the increases in capacity predicted from Equation (4.3).

4.8. Effective stress paths above and below plates

The effective stress and voids ratio paths for soil elements located in the mobilised shear zones above and below the plate highlight the different soil responses when the two-way and one-way consolidation mechanisms occur. Fig. 15a and b compare the effective stress paths for preloads of $P = 0.3$ and 0.5. When the preload is applied, only minor changes in effective stress occur. During consolidation, the effective stress rises above the anchor but falls below the anchor, which is consistent with pore pressure dissipation following the imposed changes in total stress. For the higher preload, the effective stress reduces close to zero, which is accompanied by a large increase in voids ratio, representing the gap formation. Consequently, the majority of the preload is instead carried by a gain in effective stress above the plate. For $P = 0.3$ the mean effective stress increases by 60 kPa, whereas for $P = 0.5$ the gain in p' is disproportionally larger, at ~ 200 kPa.

During the subsequent loading to failure, all stress paths move towards the critical state line, with strengthening evident above the plate in both cases, in proportion to the gain in effective stress. Beneath the plate the mobilised strength is essentially zero for $P = 0.5$. These final stress states are consistent with the higher undrained strengths and lower void ratios shown in Fig. 11a and b.
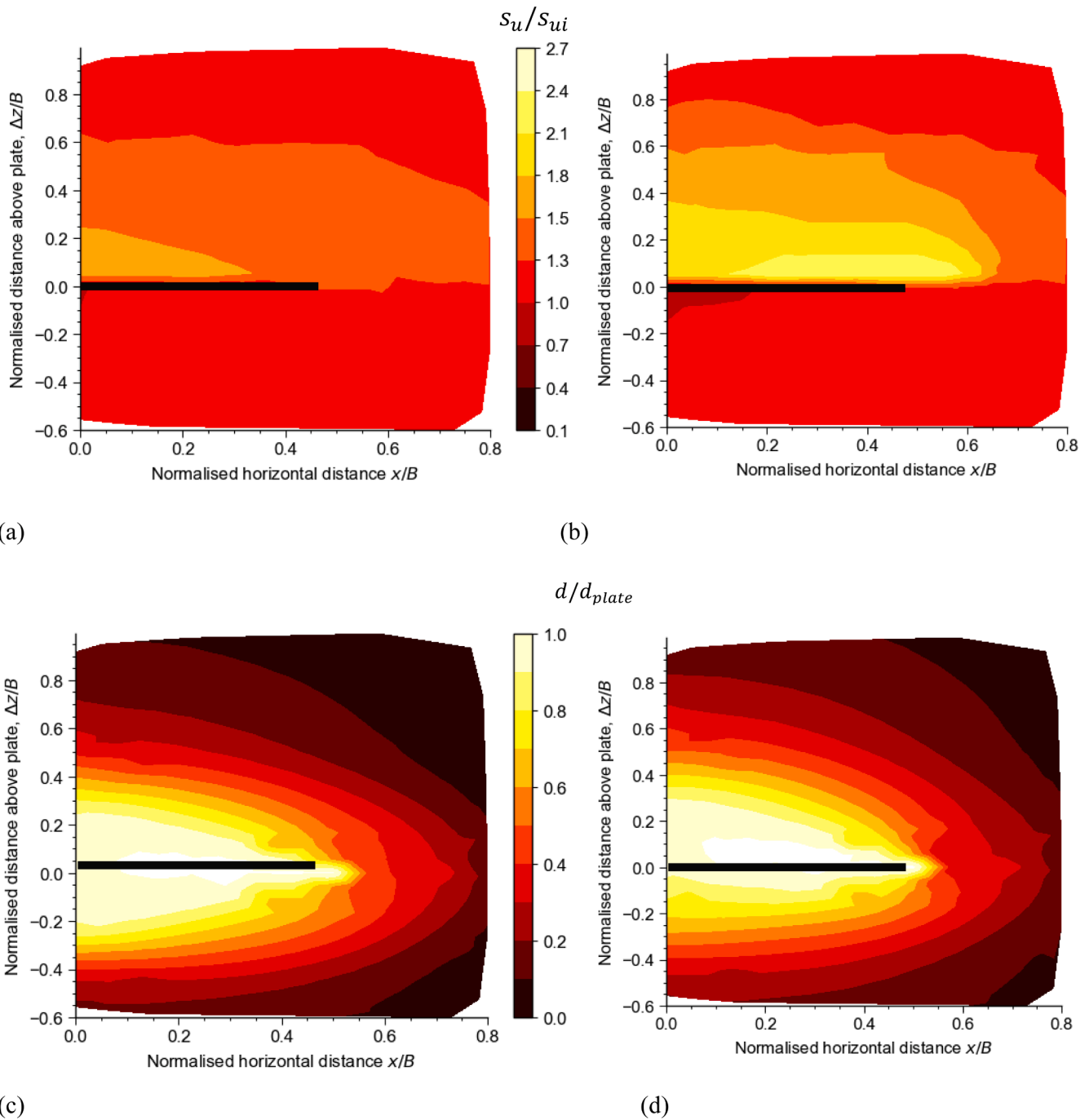
4.9. Symmetry of failure mechanism

The overall gains in plate capacity shown in Fig. 7 are different due to the net effects of the changes in the undrained strengths in the deforming soil above and below the plate shown in Fig. 9. The gains are influenced by the changing shape of the failure mechanism, as well as the changes in soil strength. One measure of the shape of the failure mechanism is the symmetry about the anchor plane, which can be quantified by comparing the weighted deformation in the soil above and below the plate, using the ratio, S:

$$S = \frac{\left(\int_{vol,above} \Delta \epsilon_p \, dv\right)}{\int_{vol,below} \Delta \epsilon_p \, dv} \tag{4.11}$$

where S represents the symmetry of the mechanism, $\Delta \epsilon_p$ is the plastic strain increment when V_{cu} is mobilised, weighted by the volume of each element, dv, within the domain volume either above or below the plate. A value of S greater than unity means there is greater deformation above the plate compared to below, and vice versa. Fig. 16 shows the variation in S with preload, P. In addition, Fig. 17 shows contour plots of the normalised undrained strengths, s_u/s_{ui} (where s_{ui} is the initial undrained strength, and s_u is the consolidated value) and the soil displacements (normalised by the plate displacement), d/d_{plate}, when V_{cu} is mobilised, for $P = 0.4$ and 0.6.

For low preload levels, Fig. 16 shows that slightly greater deformation occurs beneath the plate ($S < 1$), reflecting that the deformation concentrates slightly in the softening soil. However, for higher preload levels, a hardened zone of soil has formed immediately above the plate (Fig. 17b compared to 17a). This causes the deformation to extend through a larger zone in this region – as evidenced by the larger zone of

Fig. 19. Comparison of failure mechanisms for different preloads ($R = 0.22$) in pre-failed simulations: Strength contours for (a) $P = 0.4$ and (b) $P = 0.6$; Displacement zones for (c) $P = 0.4$ and (d) $P = 0.6$.

high displacement above the plate in Fig. 17d compared to Fig. 17c. The mobilised failure mechanism leaves this hardened zone relatively un-deformed, and instead, a larger zone of shearing and soil flow is created outside of the hardened zone.

4.10. Variation case: Anchor pre-failure

Finally, a variation case exploring the influence of pre-failing the anchor is explored, to represent certain types of practical situations, including installation by pulling into position. This variation case ex-amines the influence of the pore pressure generated by pre-failure on the subsequent preload-induced consolidation. Some model tests and nu-merical simulations of embedded anchors or 'spudcan'-type embedded

foundations shown that the installation process influences the capacity (Zhou et al. 2020; Ragni et al., 2017). In these cases, the anchor has been pulled or pushed into position through the soil prior to the preloading stage. This pre-failure process causes shearing and creates excess pore pressure around the anchor, prior to the preloading phase.

The variation case analyses for pre-failed anchors involved the following steps:

(a) establishment of the in-situ stress conditions
(b) vertical displacement of the anchor, mobilising V_{uu}
(c) immediate removal of the force on the anchor (i.e. applying $V = 0$),

(d) a consolidation period, sufficient for full excess pore pressure dissipation

(e) preloading the foundation with V_p

(f) a consolidation period, sufficient for full excess pore pressure dissipation

(g) vertical displacement causing undrained vertical bearing failure, mobilising V_{cu}

This pre-shearing stage resulted in higher residual undrained strengths in the soil around the plate before the preloading stage and at the end of the final shear stage as shown in Fig. 18a. This is consistent with the lower void ratios in the compressed soil region above the plate as shown in Fig. 18b. Less asymmetry developed in the mobilised failure mechanisms in the pre-failure simulations as shown by the open markers in Fig. 16. The soil mechanisms visualised in Fig. 19 show a larger zone of increased undrained soil strength above the plate and a smaller zone of decreased undrained soil strength beneath the plate.

Overall, this pre-failure process, with two loading and consolidation events, resulted in slightly larger gains in capacity and average mobilised undrained strengths, by $\sim 5\%$, shown by the additional cases marked in Figs. 7 and 10.

5. Conclusions

This numerical study investigated the coupled effects of consolidation and strength gain on the capacity of deeply-embedded plate anchors subjected to sustained preload. The resulting gains in anchor capacity provide a basis for more efficient anchoring system design and have been summarised into a simple analytical expression that can be used to estimate gains in anchor capacity for any preload level. The increase in capacity depends whether a water-filled gap forms beneath plate, which is controlled by the preload level and the soil undrained strength ratio.

At lower preloads, no gap forms and the preload is carried equally by compression above the plate and an increment of tension below. The resulting gains in capacity are<5 % which is significantly less than for preloaded surface footings under comparable preloads. Similar but opposite changes in total and effective stress occur above and below the plate during this symmetric consolidation process.

Beyond a preload threshold, a gap forms beneath the plate during consolidation due to the effective stress falling to zero. Consequently, levels of preload beyond this threshold lead to an asymmetric consolidation process, where the majority of the uplift preload is carried through compression of the soil above the plate. This leads to a zone of hardened soil above the plate, a change in the subsequent failure mechanism, and a higher gain in anchor capacity.

A criterion for gap formation is identified which involves the soil undrained strength ratio, R, as well as the preload level as a proportion of the initial capacity. This criterion leads to a simple basis for estimating the bi-linear relationship between preload and gain in undrained capacity due to consolidation and gap formation.

CRediT authorship contribution statement

K.A. Kwa: Conceptualization, Methodology, Software, Validation, Formal analysis, Investigation, Writing – original draft, Writing – review & editing, Visualization, Funding acquisition. **D.J. White:** Conceptualization, Methodology, Software, Validation, Formal analysis, Investigation, Writing – original draft, Writing – review & editing, Visualization, Funding acquisition, Supervision, Resources.

Declaration of Competing Interest

The authors declare that they have no known competing financial interests or personal relationships that could have appeared to influence the work reported in this paper.

Data availability

Data will be made available on request.

References

Acosta-Martinez, H.E., Gourvenec, S.M., 2006. One-dimensional consolidation tests on kaolin clay. Centre for Offshore Foundation Systems. The University of Western Australia, Crawley, Australia research report GEO: 06385.

Aubeny, C., 2017. Geomechanics of Marine Anchors. CRC Press.

Bhattacharya, P., Kumar, J., 2015. Uplift capacity of strip and circular anchors in soft clay with an overlay of sand layer. Geotech. Geol. Eng. 33 (6), 1475–1488.

Bhattacharya, P., Roy, A., 2016. Improvement in uplift capacity of horizontal circular anchor plate in undrained clay by granular column. Geomech. Eng. 10 (5), 617–633.

Biot, M.A., 1956. General solutions for the equations of elasticity and consolidation for porous material. J. Appl. Mech. 23 (2).

Blake, A.P., O'Loughlin, C.D. and Gaudin, C., 2010. Setup following keying of plate anchors assessed through centrifuge tests in kaolin clay. In Proceedings of the 2nd International Symposium on Frontiers in Offshore Geotechnics, Perth, Australia (pp. 8-10).

Blake, A.P., O'Loughlin, C.D., Gaudin, C., 2015. Capacity of dynamically embedded plate anchors as assessed through field tests. Can. Geotech. J. 52 (1), 87–95.

Cao, J., 2003. Centrifuge modelling and numerical analysis of the behaviour of suction caissons in clay. Memorial University of Newfoundland). Doctoral dissertation,.

Cerfontaine, B., White, D.J., Kwa, K.A., Gourvenec, S.M., Knappett, J.A., Brown, M.J., 2023. under review). Anchor geotechnics for floating offshore wind: current technologies and future innovations. Ocean Eng.

Chen, X.J., Fu, Y., Liu, Y., 2022. Random finite element analysis on uplift bearing capacity and failure mechanisms of square plate anchors in spatially variable clay. Eng. Geol. 304, 106677.

Colliat, J.L., Colliard, D., 2010. Set-up of suction piles in deepwater Gulf of Guinea clays. In: Frontiers in Offshore Geotechnics II. CRC Press, pp. 741–746.

Feng, X., Gourvenec, S., 2015. Consolidated undrained load-carrying capacity of subsea mudmats under combined loading in six degrees of freedom. Géotechnique 65 (7), 563–575.

Gaone, F.M., Gourvenec, S., Doherty, J.P., 2018. Large-scale shallow foundation load tests on soft clay–At the National Field Testing Facility (NFTF), Ballina, NSW, Australia. Comput. Geotech. 93, 253–268.

Gaudin, C., O'Loughlin, C.D., Randolph, M.F., 2006. New insights from model tests of foundation and anchoring systems in offshore geomechanics. In: Proc. 6th Int. Conf. on Physical Modelling in Geotechnics. Balkema), (Rotterdam, pp. 47–62.

Gourvenec, S., Randolph, M., 2003a. Effect of strength non-homogeneity on the shape of failure envelopes for combined loading of strip and circular foundations on clay. Géotechnique 53 (6), 575–586.

Gourvenec, S., Randolph, M., 2003b. Bearing capacity of a skirted foundation under VMH loading. In: ASME 2003 22nd International Conference on Offshore Mechanics and Arctic Engineering. American Society of Mechanical Engineers Digital Collection, pp. 413–416.

Gourvenec, S., Randolph, M.F., 2010. Consolidation beneath circular skirted foundations. Int. J. Geomech. 10 (1), 22–29.

Gourvenec, S.M., Vulpe, C., Murthy, T.G., 2014. A method for predicting the consolidated undrained bearing capacity of shallow foundations. Géotechnique 64 (3), 215–225.

Gourvenec, S. (2020) Whole-life geotechnical design: What is it? What's it for? So what? And what next? Proc. 4th International Symposium on Frontiers in Offshore Geotechnics, Austin, Texas, USA, Ed. Westgate, Z., ASCE Geo-Institute and DFI, ISBN: 978-0-9763229-4-8.

Han, C., Wang, D., Gaudin, C., O'Loughlin, C.D., Cassidy, M.J., 2016. Behaviour of vertically loaded plate anchors under sustained uplift. Géotechnique 66 (8), 681–693.

Khatri, V.N., Kumar, J., 2009. Vertical uplift resistance of circular plate anchors in clays under undrained condition. Comput. Geotech. 36 (8), 1352–1359.

Lehane, B.M. and Gaudin, C., 2005. Effects of drained pre-loading on the performance of shallow foundations on overconsolidated clay. International 24th International Conference on Offshore Mechanics and Arctic Engineering.

Lehane, B.M., Jardine, R.J., 2003. Effects of long-term pre-loading on the performance of a footing on clay. Géotechnique 53 (8), 689–695.

Liu, F., Yi, J., Cheng, P., Yao, K., 2020. Numerical simulation of set-up around shaft of XCC pile in clay. Geomech. Eng. 21 (5), 489–501.

Maitra, S., White, D., Chatterjee, S., Choudhury, D., 2019. Numerical modelling of seepage and tension beneath plate anchors. Comput. Geotech. 108, 131–142.

Maitra, S., Chatterjee, S., White, D., Choudhury, D., 2022. Uplift resistance of buried pipelines: The contribution of seepage forces. Ocean Eng. 250, 111037.

Makrodimopoulos, A., Martin, C.M., 2007. Upper bound limit analysis using simplex strain elements and second-order cone programming. Int. J. Numer. Anal. Methods Geomech. 31 (6), 835–865.

Mana, D.S., Gourvenec, S., Randolph, M.F., 2014. Numerical modelling of seepage beneath skirted foundations subjected to vertical uplift. Comput. Geotech. 55, 150–157.

Martin, C.M. and Randolph, M.F., (2001), January. Applications of the lower and upper bound theorems of plasticity to collapse of circular foundations. In Tenth International Conference on Computer Methods and Advances in Geomechanics, Tucson, AZ, Jan (pp. 7-12).

Martin, C.M. (2003). New software for rigorous bearing capacity calculations. Proc. British Geotech. Assoc. Int. Conf. on Foundations, Dundee, pp 581-592.

Merifield, R.S., Sloan, S.W., Yu, H.S., 2001. Stability of plate anchors in undrained clay. Géotechnique 51 (2), 141–153.

Merifield, R.S., Lyamin, A.V., Sloan, S.W., Yu, H.S., 2003. Three-dimensional lower bound solutions for stability of plate anchors in clay. ASCE J. Geotechn. Geoenviron. Eng. 129 (3), 243–253.

Murff, J. D., Randolph, M. F., Elkhatib, S., Kolk, H. J., Ruinen, R., Strom, P. J., & Thorne, C. (2005, October). Vertically loaded plate anchors for deepwater applications. In Proc Int Symp on Frontiers in Offshore Geotechnics (pp. 31-48).

Nguyen, V.Q., Merifield, R.S., 2012. Two-and three-dimensional undrained bearing capacity of embedded footings. Aust. Geomech. 47 (2), 25.

O'Loughlin, C.D., Blake, A.P., Richardson, M.D., 2014. Installation and capacity of dynamically embedded plate anchors as assessed through centrifuge tests. Ocean Eng. 88, 204–213.

O'Loughlin, C.D., Blake, A.P., Gaudin, C., 2016. Towards a design method for dynamically embedded plate anchors. Géotechnique 66 (9), 741–753.

O'Loughlin, C.D., White, D.J., Stanier, S.A., 2017. Plate Anchors for Mooring Floating Facilities–A View Towards Unlocking Cost and Risk Benefits. In: Offshore Site Investigation Geotechnics 8th International Conference Proceeding, Vol. 978. Society for Underwater Technology, pp. 978–986.

Ragni, R., Bienen, B., Wang, D., Mašín, D., Cassidy, M.J., 2017. Numerical modelling of the effects of consolidation on the undrained spudcan capacity under combined loading in silty clay. Comput. Geotech. 86, 33–51.

Randolph, M.F., Gaudin, C., Gourvenec, S.M., White, D.J., Boylan, N., Cassidy, M.J., 2011. Recent advances in offshore geotechnics for deep water oil and gas developments. Ocean Eng. 38 (7), 818–834.

Randolph, M., Gourvenec, S., 2017. Offshore geotechnical engineering. CRC Press.

Schofield, A.N., Wroth, P., 1968. Critical state soil mechanics, Vol. 310. McGraw-hill, London.

Singh, V., Chatterjee, S., 2018. Elastoplastic consolidation above and beneath strip anchors under uplift forces. Mar. Georesour. Geotechnol. 36 (5), 505–514.

Singh, V., Maitra, S., Chatterjee, S., 2017. Generalized design approach for inclined strip anchors in clay. Int. J. Geomech. 17 (6), 04016148.

Stanier, S.A., White, D.J., 2019. Enhancement of bearing capacity from consolidation: due to changing strength or failure mechanism? Géotechnique 69 (2), 166–173.

Stewart, D.P., 1992. Lateral loading of piled bridge abutments due to embankment construction. The University of Western Australia, Crawley, Australia. PhD thesis,.

Vermeer, P.A., Verruijt, A., 1981. An accuracy condition for consolidation by finite elements. Int. J. Numer. Anal. Methods Geomech. 5 (1), 1–14.

Vulpe, C., White, D.J., 2014. Effect of prior loading cycles on vertical bearing capacity of clay. Int. J. Phys. Modelling in Geotechn. 14 (4), 88–98.

Wang, D., Hu, Y., Randolph M.F. (2009). Three-dimensional large deformation finite element analysis of plate anchors in uniform clay. J Geotech Geoenviron Eng 2010; 136 2:355–65.

Wang, D., O'Loughlin, C.D., 2014. Numerical study of pull-out capacities of dynamically embedded plate anchors. Can. Geotech. J. 51 (11), 1263–1272.

White, D. and Bransby, F., (2017). Pipe–Seabed Interaction. Encyclopedia of Maritime and Offshore Engineering, pp.1-25. Wiley. ISBN: 978-1-118-47635-2.

Wood, D.M., 1990. Soil behaviour and critical state soil mechanics. Cambridge University Press.

Wroth, C.P., 1984. The interpretation of in situ soil tests. Géotechnique 34 (4), 449–489.

Yang, M., Murff, J.D., Aubeny, C.P., 2010. Undrained capacity of plate anchors under general loading. J. Geotech. Geoenviron. Eng. 136 (10), 1383–1393.

Yi, J.T., Liu, F., Zhang, T.B., Qiu, Z.Z., Zhang, X.Y., 2021. Determination of the ultimate consolidation settlement of jack-up spudcan footings embedded in clays. Ocean Eng. 236, 109509.

Yu, S.B., Hambleton, J.P., Sloan, S.W., 2015. Undrained uplift capacity of deeply embedded strip anchors in non-uniform soil. Comput. Geotech. 70, 41–49.

Zdravković, L., Potts, D.M., Jackson, C., 2003. Numerical study of the effect of preloading on undrained bearing capacity. Int. J. Geomech. 3 (1), 1–10.

Zhou, Z., O'Loughlin, C.D., White, D.J., Stanier, S.A., 2020. Improvements in plate anchor capacity due to cyclic and maintained loads combined with consolidation. Géotechnique 70 (5), 448–467.